

1 **Bias Corrected Estimation of Paleointensity (BiCEP):**
2 **An improved methodology for obtaining paleointensity**
3 **estimates**

4 **Brendan Cych¹, Matthias Morzfeld¹, Lisa Tauxe¹**

5 ¹University of California, San Diego

6 **Key Points:**

- 7 • Empirical evidence suggests that paleointensity estimates for non-ideal specimens
8 are biased.
- 9 • BiCEP is a method for estimating paleointensity for ensembles of specimens, cor-
10 recting for bias
- 11 • BiCEP produces accurate results when applied to data where the true field strength
12 is known.

Corresponding author: Brendan Cych, bcych@ucsd.edu

Abstract

The assumptions of paleointensity experiments are violated in many natural and archaeological materials, leading to Arai plots which do not appear linear and yield inaccurate paleointensity estimates, leading to bias in the result. Recently, paleomagnetists have adopted sets of “selection criteria” that exclude specimens with non linear Arai plots from the analysis, but there is little consensus in the paleomagnetic community on which set to use. In this paper, we present a statistical method we call Bias Corrected Estimation of Paleointensity (BiCEP), which assumes that the paleointensity recorded by each specimen is biased away from a true answer by an amount that is dependent a single metric of nonlinearity (the curvature parameter \vec{k}) on the Arai plot. We can use this empirical relationship to estimate the recorded paleointensity for a specimen where $\vec{k} = 0$, i.e., a perfectly straight line. We apply the BiCEP method to a collection of 30 sites for which the true value of the original field is well constrained. Our method returns accurate estimates of paleointensity, with a higher level of accuracy and precision than the strict CCRIT selection criteria, and with higher accuracy and similar precision to the modified PICRIT03 criteria. The BiCEP method has a significant advantage over using these selection criteria because it achieves these accurate results without excluding large numbers of specimens from the analysis.

Plain Language Summary

Paleomagnetists perform experiments on rocks and pottery sherds to estimate the strength of the ancient Earth’s magnetic field (the paleointensity) through time. These make assumptions which are frequently violated, leading to bias. Quantitative metrics (selection criteria) attempt to screen out ‘bad’ data. If a particular experiment fails the criteria, the results are ignored. However, there a lack of agreement as to which set of criteria are the most important and what is considered a failure. One of these criteria quantifies the deviation from the fundamental assumption of linearity of between the ancient and laboratory magnetizations. We present a new Bayesian method called Bias Corrected Estimation of Paleointensity (BiCEP), in which we assume that the estimated paleointensity depends on this deviation. We can then use this dependency to correct the paleointensity made on an ensemble of specimens with differing deviations from ideal behavior. This allows us to calculate accurate estimates of the ancient magnetic field, without ignoring results from non-ideal specimens. We test BiCEP on paleomagnetic data for which we the original field strength is well constrained. BiCEP recovers the field strength as precisely and slightly more accurately than the best performing set of selection criteria we tested.

1 Introduction

Estimates of the strength of the ancient Earth’s magnetic field are currently made by performing experiments that compare the natural remanent magnetization (NRM) acquired by a specimen while cooling in the Earth’s field, to a remanence known as thermal remanent magnetization (TRM) acquired by the specimen while cooling in a known laboratory field. Such experiments include the Königsberger-Thellier-Thellier (KTT) family of experiments (Königsberger, 1938; Thellier & Thellier, 1959), the Shaw family of experiments (Shaw, 1974), and the multi-specimen family of experiments (Hoffman et al., 1989), among others. All of these experimental families make assumptions about the relationship between the magnetic field and the remanent magnetization which may or may not be applicable (see the review by Tauxe & Yamazaki, 2015). In this paper, we will focus on the KTT family of experiments.

KTT family of experiments involve a double heating protocol in which a specimen is heated two or more times to a series of temperatures up to the Curie Temperature. At each temperature, the specimen is cooled in two different fields. This has the effect

63 of replacing the NRM with a TRM acquired in a known laboratory field. Data from KTT-
 64 type experiments are normally represented by the Arai diagram (Nagata et al., 1963),
 65 which plots the NRM magnetization remaining at each temperature step against the mag-
 66 netization imparted in the laboratory (often referred to as partial TRM or pTRM). The
 67 ratio of these two magnetizations, as represented by the slope of the best fitting line to
 68 the Arai plot data, is generally taken to be the ratio of the two magnetizing fields (an-
 69 cient, B_{anc} and laboratory, B_{lab}).

70 KTT-type experiments rely on several assumptions which are frequently violated
 71 in paleointensity experiments. These include thermochemical alteration of specimens which
 72 may lead to the production of new magnetic minerals, and an assumption known as reci-
 73 procity, which requires that the blocking temperature (the temperature below which grains
 74 retain their magnetization after an external field is removed) is the same as the unblock-
 75 ing temperature (the temperature above which grains equilibrate with the external field).

76 The reciprocity assumption of Thellier and Thellier (1959) is fundamental to Néel's
 77 theory for uniaxial single domain grains (Néel, 1949). Néel theory assumes that the elec-
 78 tronic spins within magnetic grains are fully aligned, and that the alignment is in one
 79 of two directions along an energetically favorable 'easy' axis. In zero field, there is no pref-
 80 erence for either direction, but in the presence of a field there is a slight preference for
 81 the direction along the easy axis with the smallest angle to the applied field. If the reci-
 82 procity assumption is met, then the energy required for the magnetization to change di-
 83 rections along the easy axis is always the same regardless of whether the specimen is cooled
 84 from higher temperature (blocking) or heated from room temperature (unblocking) and
 85 the two temperatures are identical.

86 By assuming that electronic spins within magnetic grains are fully aligned, Néel
 87 theory fails to take into account a term in the magnetic energy of grains which causes
 88 deviations from full alignment, resulting in structures such as the vortex state of, e.g.,
 89 Williams and Dunlop (1989). Although this effect is present in nearly all magnetic grains,
 90 it is insignificant over short length scales (10s of nm) and so uniaxial single domain the-
 91 ory may be a reasonable approximation for smaller, elongate grains. Specimens in pa-
 92 leointensity experiments contain mixtures of grains with different sizes and shapes and
 93 a specimen used for paleointensity is likely to include grains for which the applicability
 94 of single domain theory does not hold.

95 Failure of reciprocity and other fundamental assumptions embedded in the KTT
 96 family of experiments (laid out by e.g., Thellier & Thellier, 1959) provides a challenge
 97 for those analyzing paleointensity data. Paleomagnetists generally use a set of selection
 98 criteria which reject an intensity result if the NRM and pTRM data behave in a way which
 99 deviate from single domain theory (linear on the Arai plot, see Figure 1a) by more than
 100 some arbitrarily chosen threshold value. This is because data that contain a large pro-
 101 portion of non single domain-like grains or which otherwise violate the assumptions of
 102 the experiment are likely to give biased results (Tauxe et al., 2021). Selection criteria
 103 generally operate in a binary way, with specimens either being 'accepted' or 'rejected'
 104 from the estimation of the site mean, where 'site' is the collection of specimens assumed
 105 to have cooled in identical external magnetic fields (say, a lava flow or ceramic fragment).

106 Figure 1 gives a demonstration of biased results in specimens from prepared mag-
 107 netite powders of increasing grain size that were magnetized in a $60 \mu\text{T}$ field (Krása et
 108 al., 2003). If all assumptions of Thellier and Thellier (1959) were obeyed, we would ex-
 109 pect the best fitting lines to data on Arai plots to give a range of values distributed closely
 110 about a mean of $60 \mu\text{T}$. As the grain size of the powder increases, the Arai plot becomes
 111 more curved and the best fitting line to the Arai plot yields a progressively lower inten-
 112 sity estimate. As all the paleointensities estimated from the curved plots are below the
 113 expected value, the estimate for the ensemble can be biased, with the high temperature
 114 segment having an even lower mean value, and the low temperature segment having a

high mean value. The data of Tauxe et al. (2021) also demonstrate downward curved Arai plots in natural samples are biased so this problem may effect many of the results compiled in paleointensity databases like the MagIC database (Tauxe et al., 2016) or PINT (Biggin, 2010).

The curvature of an Arai plot can be quantified using the curvature criterion (\vec{k}) of Paterson (2011) (see also Paterson et al., 2014). Curvature is calculated using the reciprocal of the radius of a circle fit to scaled Arai plot data (see Section 2.2.1). While there is no theoretical basis for a circular fit (as opposed to the linear fit, which is firmly rooted in Néel theory), it is a useful approximation that we will use in this paper.

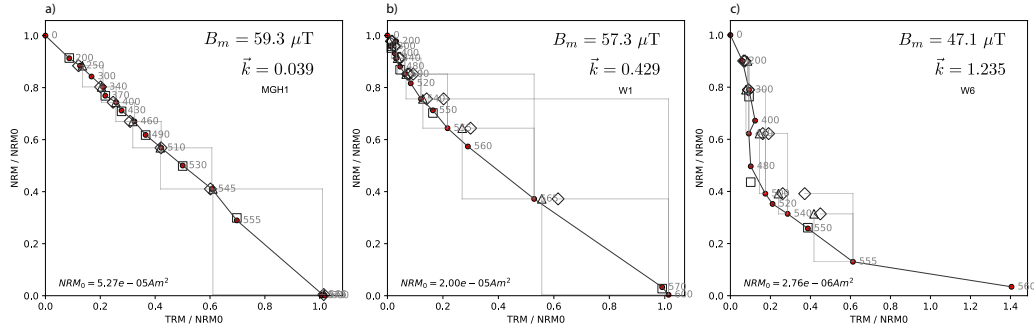


Figure 1. Arai plots from prepared magnetite powders given a TRM in a 60 μT field (Krása et al., 2003). The curvature criterion, \vec{k} (Paterson, 2011) and specimen level paleointensity estimate B_m estimated from fitting a line to the entire Arai plot are plotted on the figure as text. The grain size of the magnetite powders increases from left to right. The coarser grains have non ideal domain state, leading to curved Arai plots and estimates of paleointensity which are biased to lower values than the expected 60 μT . a) Nominal grain size of 23 nm. b) Mean grain size of 70 nm. c) Mean grain size of 12.1 μm .

The practice of using binary (pass/fail) selection criteria is problematic for many reasons. Paleomagnetic specimens generally contain magnetic carriers which span a range of grain sizes and may or may not conform to the assumptions of the method. In addition, micromagnetic simulations (e.g., Williams and Dunlop (1989); Nagy et al. (2017)) demonstrate that the change in magnetic domain state with grain size is a continuum, and so one individual grain’s behaviour may be more or less ideal than any other’s. With binary pass/fail criteria, the distinction between ‘good’ and ‘bad’ data must be assessed with an arbitrary threshold value, which does not reflect the range of behaviors within both groups. Consequently there are a large number of selection criteria in common use (over 40 in Paterson et al., 2014), most of which have some empirical rationale, but there is little agreement on which set to use or their threshold values.

In this paper, we describe a new approach for paleointensity estimation that treats the quality of paleointensity data as a continuum. We assume that paleointensities become more biased as specimens’ magnetic behaviors become more non-ideal and their Arai plots become less linear. By allowing the data interpretation for specimens to be based on the shape of their Arai plots, we are able to obtain unbiased estimates of paleointensity without the need for many specimen level (binary) selection criteria. We call this method the ‘Bias Corrected Estimation of Paleointensity’ or BiCEP. In the next section, we develop a Bayesian approach to obtain accurate paleointensity estimates with realistic uncertainties, using k as a metric of bias, and show how to combine data at the site level. In Section 3 we compare results from the BiCEP method to those of more tra-

145 additional selection criteria based approaches. We discuss the results in Section 4 and sum-
146 marize our conclusions in Section 5. Accompanying this paper, we release a Graphical
147 User Interface (GUI) which can apply the BiCEP method to MagIC formatted data. Links
148 and instructions on how to access the code can be found in Appendix 6.3.

149 2 Methods

150 2.1 Accounting for bias in paleointensity experiments

151 Paleomagnetists determine the paleointensity for a site by performing a Thellier-
152 type double heating experiment on multiple specimens from that site. According to the
153 theory for single domain grains (assuming no alteration of the specimen during heating),
154 the ratio of NRM lost to pTRM gained is the ratio of the ancient field to the laboratory
155 field. If the specimen conforms to theory, the Arai plot data will fall along a line the slope
156 of which is equal to the ratio of ancient to the laboratory field (see Figure 1a).

157 We expect that the field strength predicted by the slope of the line on the Arai plot
158 for each specimen (here called B_m) will be distributed about the true (expected) ancient
159 field (B_{exp}) at the site with a Gaussian distribution. However, rarely do a set of spec-
160 imens from a site all produce linear Arai plots that are easily interpretable. For exam-
161 ple, interpretation of data from specimens with magnetic grains exhibiting non single do-
162 main magnetic domain states produce non-linear Arai plots which violate the assump-
163 tions of the method (e.g., Dunlop & Özdemir, 2001). Fitting lines to the data on such
164 Arai plots often produces estimates of paleointensity which are biased (see Figure 1c, Krása
165 et al., 2003), which in turn would bias site level estimates.

166 Paleomagnetists generally deal with non-ideal data by using certain quantitative
167 criteria chosen to eliminate results suffering from one or more pathologies (Paterson et
168 al., 2014). If a particular criterion calculated for a specimen exceeds some threshold value,
169 then the specimen is excluded from the analysis. In this paper, we present an alterna-
170 tive approach in which we allow for specimens to behave in a non-ideal (non-linear) fash-
171 ion when considering how specimen intensity estimates are distributed about a site mean
172 and weight the contribution of individual specimen estimates according to linearity. Un-
173 der such a scheme, we start by predicting a bias for each specimen, and the specimens
174 with the smallest predicted bias most strongly determine the paleointensity at that site.
175 In this way, biased specimens do not strongly affect our site intensity estimate, as they
176 are down-weighted, yet provide useful constraints on the uncertainty.

1991-1992 Eruption Site	10.1029/2005GC001141	lava flow	9.8	-104.3	1991	36.2	53
hw108	10.1016/j.pepi.2014.12.007	lava flow	19.9	-155.9	1859	39.3	23
hw123	10.1016/j.pepi.2014.12.007	lava flow	19.1	-155.7	1907	37.7	12
hw126	10.1016/j.pepi.2014.12.007	lava flow	19.7	-155.5	1935	36.4	13
hw128	10.1016/j.pepi.2014.12.007	lava flow	19.3	-155.9	1950	36.2	26
hw201	10.1016/j.pepi.2014.12.007	lava flow	19.4	-155.0	1990	35.2	12
hw226	10.1016/j.pepi.2014.12.007	lava flow	19.6	-155.5	1843	39.9	11
hw241	10.1016/j.pepi.2014.12.007	lava flow	19.5	-155.8	1960	36.0	18
BR06	10.1016/j.pepi.2007.10.002	brick	60.1	24.9	1906	49.7	3
P	10.1029/2010JB007844, 2011	lava flow	19.3	-102.1	1943	44.6	36
VM	10.1029/2010JB007844, 2013	lava flow	40.8	14.5	1944	43.8	18
BBQ	10.1029/93jb01160	submarine lava flow	9.8	-104.3	1990	36.2	12
rs25	10.1016/j.epsl.2009.12.022	synthetic	N/A	N/A	N/A	30.0	5
rs26	10.1016/j.epsl.2009.12.022	synthetic	N/A	N/A	N/A	60.0	5
rs27	10.1016/j.epsl.2009.12.022	synthetic	N/A	N/A	N/A	90.0	10
remag-rs61	10.1016/j.epsl.2011.08.024	synthetic	N/A	N/A	N/A	40.0	6
remag-rs62	10.1016/j.epsl.2011.08.025	synthetic	N/A	N/A	N/A	60.0	6
remag-rs63	10.1016/j.epsl.2011.08.024	synthetic	N/A	N/A	N/A	80.0	5
remag-rs78	10.1016/j.epsl.2011.08.025	synthetic	N/A	N/A	N/A	20.0	4
kf	10.1111/j.1365-246X.2012.05412.x	lava flow	65.7	-16.8	1984	52.0	3
Hawaii 1960 Flow	10.1046/j.1365-246X.2003.01909.x	lava flow	19.5	-155.8	1960	36.0	22
SW	10.1016/j.pepi.2008.03.006	lava flow	31.6	-130.6	1946	46.4	19
TS	10.1016/j.pepi.2008.03.006	lava flow	31.6	-130.6	1914	47.8	53
ET1	10.1016/j.epsl.2007.03.017	basaltic lava	37.8	15.0	1950	43.3	3
ET2	10.1016/j.epsl.2007.03.017	basaltic lava	37.8	15.0	1979	44.1	2
ET3	10.1016/j.epsl.2007.03.017	basaltic lava	37.8	15.0	1983	44.2	4
Synthetic60	10.1016/S1474-7065(03)00122-0	synthetic	N/A	N/A	N/A	60.0	7
LV	10.1029/2009JB006475	Lithic Clasts	-23.4	67.7	1993	24.0	45
MSH	10.1029/2009JB006475	Lithic Clasts	46.2	-122.2	1980	55.6	19
FreshTRM	10.1029/2018GC007946	remagnetized/synthetic	N/A	N/A	N/A	70.0	24

Table 1. Table of sites used for analysis in this study, including original study locations, latitude, longitude and year of magnetization (where applicable), expected field at that location (B_{exp}), number of specimens used for analysis at that site M . Lat.: site latitude ($^{\circ}$ N). Long. site longitude ($^{\circ}$ E. N/A: Not Applicable (Synthetic)).

To predict the amount of bias a specimen is likely to have, we require a proxy for bias in paleointensity experiments. For this we use the curvature criterion \vec{k} of Paterson (2011) (see Section 2.2.1). There are several reasons that make this criterion a useful proxy for bias in paleointensity experiments:

- Specimens that are highly linear have, by definition, low values for $|\vec{k}|$ and will generally give unbiased paleointensity estimates (e.g., Cromwell et al., 2015).
- By contrast, specimens with higher $|\vec{k}|$ yield biased paleointensities, with the magnitude of the bias generally increasing with the magnitude of $|\vec{k}|$ (e.g., Tauxe et al., 2021).
- $|\vec{k}|$ has an empirical correlation with magnetic grain size (Paterson, 2011).

To predict bias, we can use a method by which we minimize the misfit to a model assuming that B_m is linearly related to \vec{k} for all specimens. In other words, we say that:

$$B_m = B_{exp} + c\vec{k}_m + \epsilon \quad (1)$$

where m is an index reflecting the specimen number, ϵ is an error term and B_{exp} is the true value of B . Effectively, our model just becomes a linear fit between the specimen estimate B_m and \vec{k} , the y-intercept of which is the true value of the field B_{exp} and c is a slope constant. While there is no theoretical justification (yet) for why B_m would be related to \vec{k}_m , although it has been observed empirically (Figure 1 and Tauxe et al. (2021)), a linear model is the simplest one to relate the two. We demonstrate in Section 3.3 that more complex models with a quadratic and cubic fit relating B_m to \vec{k}_m perform worse than the linear model when predicting the paleointensity for sites for which the paleointensity is well constrained (historical lava flows or laboratory remanences).

Arai plot curvature is not the sole cause of bias in paleointensity experiments. In some cases, specimens with Arai plots which do not have high $|\vec{k}|$ but are still non linear (e.g., ‘zig-zagged’ as in, e.g., Yu et al., 2004), may still cause bias in paleointensity experiments. To counteract this, we use a Bayesian method of calculating \vec{k}_m and B_m which provides an uncertainty for both of these parameters. The benefit of this approach is that specimens whose Arai plots are not well fit by a line or an elliptical arc have less influence on the linear fit. Therefore, the specimens with the lowest uncertainty in \vec{k} are generally the most linear, and will have the most influence on the linear fit. Yet, for each specimen, there is a trade off between minimizing the circle fit at a specimen level and the linear fit between B_m and \vec{k} for specimens from the same site, an issue we will deal with in Section 2.2.3.

Figure 2 shows results from our method (detailed in Section 2.2) applied to several sites for which the true value of B_{anc} (here, B_{exp}) is either calculated from the International Geomagnetic Reference Field (IGRF, Thébault et al., 2015) for historical flows, or known as the NRM is a laboratory TRM imparted to the specimens. Following Equation 1, the uncertainty in the intercept value of these linear fits gives us the uncertainty for our site value of B_{anc} . In this way, we can obtain an unbiased estimate of B_{anc} without relying on arbitrary binary (accept/reject) criteria to exclude specimen results.

In the following, we detail how the specimen level circle fit \vec{k} and site level paleointensity for unknown values for B (here called B_{anc}) can be calculated. We then compare the efficacy of several different versions of our model to classical selection criteria. We do this using a data compilation from 30 sites updated from Paterson et al. (2014) and Tauxe et al. (2016) for which B_{exp} is well constrained (see Table 1 for details concerning the original publications of the data).

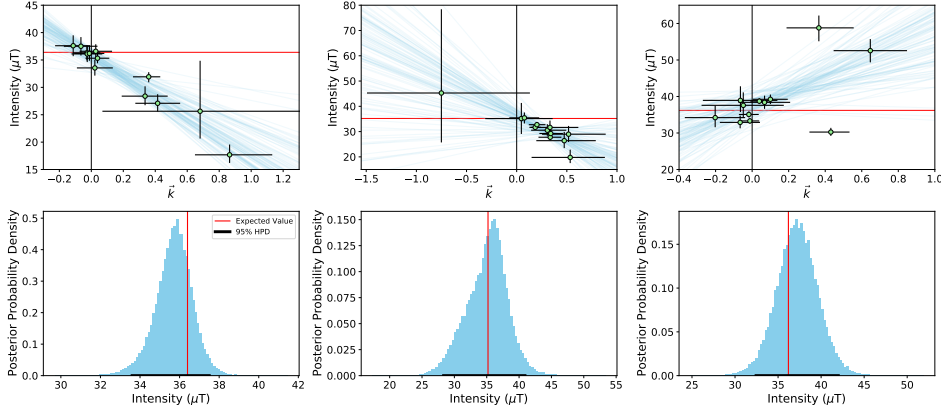


Figure 2. Example of results from the BiCEP method for several sites used as examples in this study. Lines (in blue) are fit to the values of B_m and \vec{k} for each specimen (blue dots, with uncertainties as black lines). The values of linear fits at $\vec{k} = 0$ (blue histograms) provide an unbiased estimate of the expected paleointensity value at the site from the known field (red lines). a,d) hw126. b,e) hw201. c,f) BBQ. See Table 1 for sampling and citation details and Section 3 for comparison with the expected field values, B_{est} .

222

2.2 Statistical Methodology

223

2.2.1 Estimating curvature

224

Paterson (2011) proposed a least squares fit of circles in Arai plot data. The parameter \vec{k} of Paterson (2011) is defined as the reciprocal of the radius of a best-fitting circle through the data. It is positive if the circle center is to the upper right of the Arai plot data (upward facing bow, Figure 3a) and negative if the circle center is below and to the left of the Arai plot data (downward facing bow, Figure 3b).

226

227

228

Before fitting to the Arai plot data, Paterson (2011) scales the pTRMs by the maximum pTRM to ensure that the paleointensity data are independent of the laboratory field. For estimating \vec{k} , we also subtract the minimum remaining NRM (NRM_{min}) for specimens for which full demagnetization has not been completed and we subtract the minimum pTRM ($pTRM_{min}$) for specimens for which the low temperature steps were excluded from the analysis (e.g., because of viscous remanent magnetization). This modified form is termed \vec{k}' (Paterson et al., 2014).

232

233

234

235

For the BiCEP method, we define two sets of data vectors x and y :

236

$$x_n = \frac{pTRM_n - pTRM_{min}}{pTRM_{max}}, \quad y_n = \frac{NRM_n - NRM_{min}}{NRM_0}, \quad (2)$$

237

238

239

240

241

242

where n is the index of the data point. Because scaling should be by the total (original) TRM (the NRM), we also exclude specimens whose NRM_{min} is more than 25% of the initial NRM. This is justified by the assumption that the experimenter did not carry out demagnetization to fully replace the NRM. Then, to fit a circle with center x_c, y_c and radius R to the data, we try to minimize the squared perpendicular distance d_n^2 (Figure 3a) of all the n data points to the circle edge:

$$\sum_{n=1}^N d_n^2 \quad \text{where} \quad d_n^2 = (\sqrt{(x_n - x_c)^2 + (y_n - y_c)^2} - R)^2. \quad (3)$$

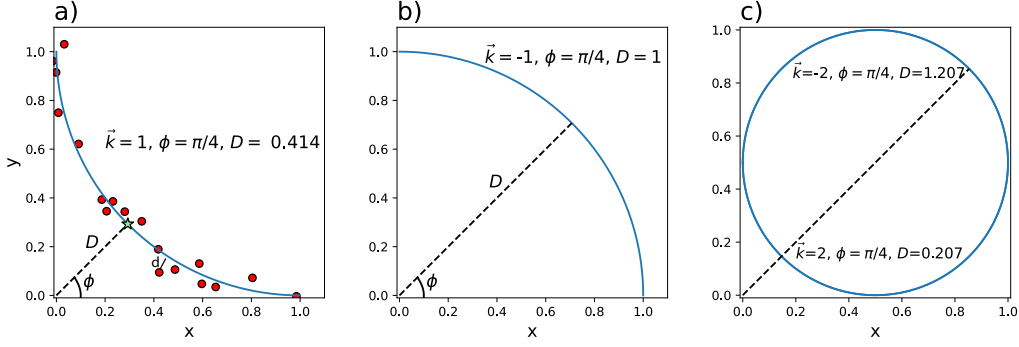


Figure 3. Example circles with different values for parameters \vec{k} and D with the same ϕ , showing how these parameters define a circle. a) Positive \vec{k} . Red dots are example data, and the green star is the intersection of D, ϕ with the circle edge (see text for definitions). d is the distance of an individual data point from the best-fit curve (blue). b) Negative \vec{k} . Note that in this case, ϕ could take any value as the circle center is at the origin, making the definition of ϕ meaningless in this case. c) Example showing how two sets of the parameters \vec{k}, ϕ, D can describe the same circle.

243 In a total least squares fit, Equation 3 would be our objective function that we would
 244 minimize. To fit circles to the Arai plot using a Bayesian method, we use Bayes' formula
 245 (Equation 4). This formula allows us to assign a probability distribution to the values
 246 of different parameters (in this case, \vec{k}_m and B_m), rather than just finding the 'best' value
 247 of the parameters. In a Bayesian context, we can simply assume that the data have some
 248 Gaussian noise distribution with some unknown standard deviation σ and apply Bayes'
 249 formula (e.g., Gelman et al., 2004):

$$P(\text{Parameters}|\text{Data}) = \frac{P(\text{Data}|\text{Parameters})P(\text{Parameters})}{P(\text{Data})}, \quad (4)$$

250 where the left hand side is the probability of the parameters given the data and the right
 251 hand side is the probability of the data given the parameters times the probability of the
 252 parameters, normalized by the probability of the data. In our case, the parameters are
 253 x_c, y_c, R and σ and our data are x and y so we rewrite Equation 4 as:

$$P(x_c, y_c, R, \sigma|x, y) = \frac{P(x, y|x_c, y_c, R, \sigma)P(x_c, y_c, R, \sigma)}{P(x, y)}. \quad (5)$$

254 The term $P(x, y|x_c, y_c, R, \sigma)$ is known as the "likelihood" and is based on the prob-
 255 ability of generating the observed data from a given set of parameters using the assumed
 256 Gaussian distribution. The term $P(x_c, y_c, R, \sigma)$ is known as the "prior" and is a prob-
 257 ability distribution for values of x_c, y_c, R and σ we consider to be reasonable before we
 258 see any data. We consider the priors on these parameters to be independent of one an-
 259 other, so we could rewrite this as $P(x_c)P(y_c)P(R)P(\sigma)$. The term $P(x, y)$ is known as
 260 the "evidence", and is simply a normalizing constant that makes the "posterior" prob-
 261 ability distribution, $P(x_c, y_c, R, \sigma|x, y)$, integrate to 1. In our application, we can sim-
 262 plify the relationship by ignoring the normalization. Furthermore, we can say from the
 263 definition of the Gaussian distribution that:

$$P(x, y|x_c, y_c, R, \sigma) = \left(\frac{1}{2\pi\sigma^2}\right)^{N/2} \exp\left(-\sum_{n=1}^N \frac{d_n^2}{\sigma^2}\right). \quad (6)$$

264 Now we have an expression for our posterior probability distribution:

$$P(x_c, y_c, R, \sigma | x, y) \propto \left(\frac{1}{2\pi\sigma^2} \right)^{N/2} \exp \left(\sum_{n=1}^N -\frac{d_n^2}{\sigma^2} \right) P(x_c, y_c, R) P(\sigma). \quad (7)$$

265 Because the actual noise distribution of the Arai plot data is quite complicated (Paterson
266 et al., 2012), we do not know the value of σ , so we use the uninformative prior $P(\sigma) \propto$
267 $\frac{1}{\sigma}$; in other words, the smaller σ , the more likely the result. We can then substitute this
268 prior into Equation 7 and integrate out σ to obtain:

$$P(x_c, y_c, R | x, y) \propto \left(\sum_{n=1}^N d_n^2 \right)^{-N/2} P(R, x_c, y_c) \quad (8)$$

269 where N is the total number of measurements considered.

270 The set of parameters x_c, y_c and R is not easy to solve for, because Equation 3 has
271 multiple local minima (see Chernov and Lesort (2005) for a more detailed discussion).
272 Consider the simple case of a specimen with a linear Arai plot; in even this simplest case,
273 there are four minima, as both R and x_c, y_c will be either positive or negative and very
274 large. To avoid this complexity, we can use instead a change of parameters similar to that
275 of Chernov and Lesort (2005) which Paterson (2011) used as a basis for the circle fit-
276 ting protocol. Based on this, we define a set of three new parameters which avoid the
277 problem of multiple minima.

278 Firstly, we require a point on the Arai plot which can be related to a unimodal dis-
279 tribution. We know that linear data will plot along the edge of a circle (the tangent),
280 so if we draw a line from the origin toward the center (x_c, y_c) (not shown), this will touch
281 the edge of the circle at some distance D (green star in Figure 3a). The angle to the hor-
282 izontal of this line we call ϕ and we can directly estimate the \vec{k} parameter of Paterson
283 (2011) using Equations 9,10,11. We can then establish equations for transforming be-
284 tween these two sets of parameters (see Appendix 6.1 for a more detailed derivation):

$$x_c = \left(D + \frac{1}{\vec{k}} \right) \cos(\phi), \quad (9)$$

$$y_c = \left(D + \frac{1}{\vec{k}} \right) \sin(\phi), \quad (10)$$

$$R = \frac{1}{|\vec{k}|}. \quad (11)$$

287 Despite this transformation, the circle fitting equation can still have multiple min-
288 ima, even with \vec{k}, D, ϕ as our parameters, as the line connecting the origin to the hor-
289 izontal touches the circle edge in two locations (see Figure 3c). However, we can use prior
290 distributions to avoid this.

291 Chernov and Lesort (2005) define a function of the data d_{max} to define the region
292 of possible values for \vec{k} :

$$d_{max} = \max_{i,j} \sqrt{(x_i - x_j)^2 + (y_i - y_j)^2} \quad (12)$$

293 Additionally, we define distance from the origin to the centroid of the data, d_{cent} :

$$d_{cent} = \sqrt{\bar{x}^2 + \bar{y}^2} \quad (13)$$

294 Using this function, we can assume that $D < 2d_{cent}$ and $|\vec{k}| < N/d_{max}$ and can de-
295 fine priors for our parameters:

$$P(D) \sim \text{Uniform}(0, 2d_{cent}), \quad (14)$$

296

$$P(\phi) \sim \text{Uniform}(0, \pi), \quad (15)$$

297 and

$$P(\vec{k}) \sim \text{Uniform}(-N/d_{max}, N/d_{max}). \quad (16)$$

298 Using these priors gives us a posterior with a single maximum in most cases, which makes
 299 the problem much easier to solve computationally.

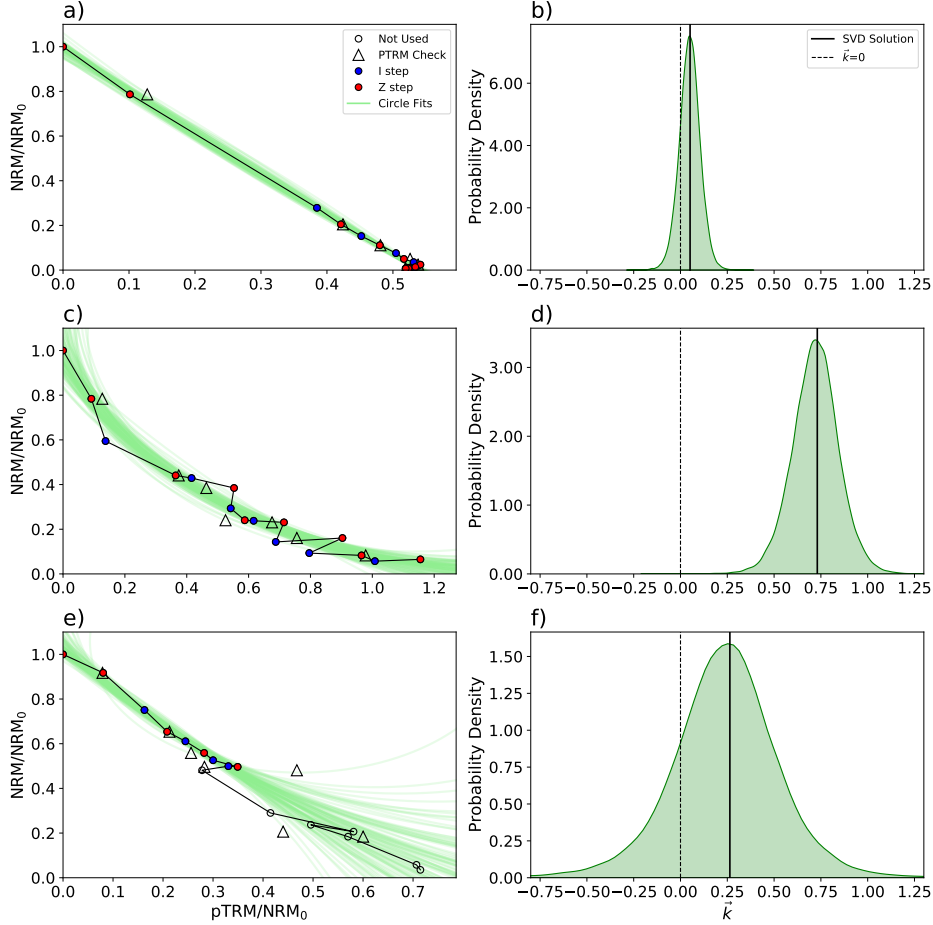


Figure 4. Examples of circle fits to Arai plots (left column) and approximate probability densities of \vec{k} (right column). Dashed lines in the left hand plots are the tangents to circles with the median values for ϕ and D . We use tangents to the circle to get an estimate for B_m as outlined in Section 2.2.2. Triangles in a),c,e) are repeated lower temperature steps (pTRM checks) that indicate alteration of magnetic minerals during the experiment when offset from the original measurements (red dots). a) Specimen hw126a1. A fit to a straight line yields a precise \vec{k} distribution with a maximum close to zero (b). c) Specimen hw126a7. A curved Arai plot with a high amount of scatter/zigzagging (left) results in a higher uncertainty in the value of \vec{k} (d). e) Specimen hw126a6. Arai plot for a specimen that underwent thermochemical alteration at high temperature. A circle fit to just the low temperature steps results in a high uncertainty in the value of \vec{k} (f).

We can now apply a Bayesian approach to estimate \vec{k} for all temperature steps for a given specimen m . It is frequently useful to choose a subset of the temperature steps (e.g., if there is evidence for multiple components of the NRM or heating related alteration, as detected by repeated lower temperature pTRM steps). When using a subset of steps, we scale by the maximum pTRM for all temperature steps and the NRM at room temperature; in this way we can predict the curvature for the part of the Arai plot that is missing. This means that interpretations based on a fraction of the Arai plot will have large uncertainties in the value of \vec{k} . Therefore, our circle fit can prioritize interpretations using the largest fraction of the NRM.

Figures 4a,c,e show circle fits sampled from the posterior distributions for specimens from site hw126 (site level results shown in Figure 2a). The probability densities of all the \vec{k} values for each specimen are plotted in Figures 4b,d,f. The plot demonstrates how a straight Arai plot (Figure 4a) produces a narrow posterior about $\vec{k} = 0$ (Figure 4b), while a curved one (Figure 4c) produces a posterior which does not contain $\vec{k} = 0$ (Figure 4d). In the example with failed pTRM checks at higher temperatures (offset triangles in Figure 4e), we exclude the data points represented by open circles and use a linear segment with only a portion of the results, the posterior distribution of \vec{k} has a larger uncertainty on the value, translating to a larger uncertainty in the bias for that specimen.

2.2.2 Obtaining a specimen level paleointensity estimate

Analogous to the case in which paleointensity estimates are made using the slope of a fitted line to the Arai plot data, we can obtain a similar “slope” value for a circular arc fit to the data. Consider the case in which the edge of the circle forms an exact line ($\vec{k}=0$, see Figure 4a). In this case, the slope of the line can be given by the tangent to the circle at the point where it intersects a line drawn from the origin (0,0) to the circle center (Figure 3a). In other words, the “slope” of the Arai plot can be estimated as $\cot \phi$, which gives the tangent to the circle. We can then turn this into an intensity estimate B_m using the formula:

$$B_m = \frac{B_{lab} \cot(\phi)}{\text{pTRM}_{max}}, \quad (17)$$

where B_{lab} is the laboratory field used to impart a pTRM to the specimen.

We now have a way of obtaining estimates for B_m and \vec{k}_m for each specimen. We use the methodology laid out in Sections 2.2.1 and 2.2.2 to plot the median value of the posterior for these parameters (with error bars) in Figure 5a, and examples of circle fits in Figures 5c, e, g. For specimens with values of \vec{k} that are approximately 0 (Figure 5g), the B_m values are quite accurate. There appears to be a bias for specimens with large \vec{k} , with the amount of bias increasing as \vec{k} increases. In this example, large positive values of \vec{k} lead to a large underestimates of B_m while negative values of \vec{k} lead to overestimates of B_m (although small in this example).

2.2.3 Obtaining a site level paleointensity estimate

The main problem with the method presented thus far is that we still do not have a way of obtaining an estimate for B_{anc} , the unknown value at the site level. However, in Figure 5a there appears to be a dependence between \vec{k}_m and B_m as suggested earlier, with most of the specimens showing a quasi-linear relationship (the only exception being the point labeled e) whose Arai plot is shown in Figure 5e) and suggests there is a great deal of uncertainty in the value of \vec{k} itself. Because of this, we can modify our model slightly by imposing the extra restriction that B_m must be linearly dependent on \vec{k}_m (with noise) using Equation 1 (substituting B_{anc} for the unknown value of B_{est}).

346 Previous papers have assumed that B_{anc} for selected specimens follows a Gaussian
 347 distribution and we can also make this assumption here. In the following, we will show
 348 how this modification can shift results from specimens that are offset from the linear re-
 349 lationship toward the line (as in the point labeled ‘f’ in Figure 5b) and produce mod-
 350 els (shown as blue lines) that estimate all of our B_m . We can then use the resulting mod-
 351 els to estimate the probability distribution for B_m as:

$$P(B_m|k_m, B_{anc}, \sigma_{site}, c) = \frac{1}{\sqrt{2\pi\sigma_{site}^2}} \exp\left(-\frac{(B_{anc} + c\vec{k}_m - B_m)^2}{2\sigma_{site}^2}\right). \quad (18)$$

352 Now we can combine our expressions for B_m and \vec{k}_m (Equations 17, Sections 2.2.1
 353 and 2.2.2) with the new constraint of a linear relationship between B_m and \vec{k}_m (Equa-
 354 tion 18). This allows us to obtain an expression for the site level intensity estimate B_{anc} :

$$355 \begin{aligned} &P(B_{anc}, \sigma_{site}, c, B_m, k_m, D_m|x_m, y_m) \propto \\ &P(x_m, y_m|k_m, D_m, B_m)P(B_m|k_m, B_{anc}, \sigma_{site}, c)P(B_{anc}, \sigma_{site}, c)P(D_m, k_m). \end{aligned} \quad (19)$$

356 Equation 19 may look complicated, but we defined each of the terms already. The ben-
 357 efit of this treatment is that we can obtain $P(x_m, y_m|k_m, D_m, B_m)$ from our circle fit-
 358 ting in Equation 8 (see also Appendix 6.1). We defined $P(B_m|k_m, B_{anc}, \sigma_{site}, c)$ in Equa-
 359 tion 18. The values of \vec{k} and B_m for each specimen needed to fit both of these terms. This
 360 means that specimens with large scatter in their Arai plots (those which have Arai plots
 361 that are not fit well by a line or a circle) are more strongly affected by the site level fit
 362 B_{anc} , and therefore by the specimens with more linear (or circular) Arai plots. Conversely,
 363 those specimens with a small uncertainty in \vec{k} or B_m are tightly constrained by the Arai
 364 plot fit and so have more control over the fit at the site level.

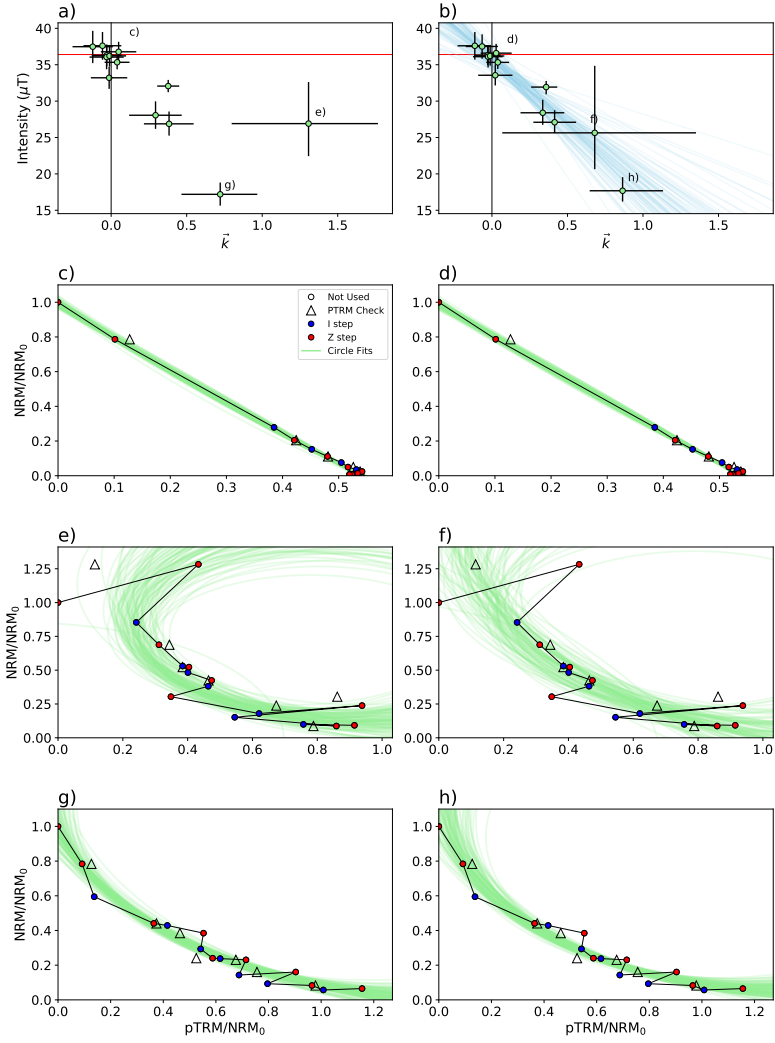


Figure 5. Examples demonstrating how the predicted \vec{k} and B_m for each specimen are modified for a site by using a hierarchical model (Equation 14). The left column shows samples from the posterior for an “unpooled” model where we estimate B_m and \vec{k}_m independently. The right column shows samples from the posterior for the BiCEP method where we assume a linear relationship between B_m and \vec{k}_m . a) Red horizontal line is B_{exp} (hw126, see Table 1). 95% credible intervals for \vec{k}_m and B_m are plotted using black error bars, with the medians as green points. b) Representative MCMC samples from the posterior distribution are plotted as blue lines assuming that the individual specimen values B_m follow the relationship stated in Equation 14. Note that the higher curvature specimens with large uncertainty in \vec{k} follow a linear trend away from B_{exp} . c),e),g): [Symbols same as in Figure 4.] Arai plots of particular specimens are shown with circle fits sampled from the posterior of the unpooled model shown in a) and plotted in green. In d), f), h), same specimens as in c), e), g) but using the posterior of the BiCEP model in b). Note that there is little change in the specimen in d) for which a close fit to the data is possible, but in f) and h) the curvature (and intensity) of the specimen are modified to fit the line better.

365 The other two terms on the right side of Equation 19 ($P(B_{anc}, \sigma_{site}, c)P(D_m, k_m)$),
 366 are priors. $P(D_m, k_m)$ were defined in Equations 14 and 16 respectively. Now, we need
 367 to define priors for $P(B_{anc}, \sigma_{site}, c)$. For this purpose, we use a poorly constrained prior
 368 for the slope, c , where $P(c) \propto 1$. Although this is not a probability distribution, the
 369 resulting posterior distribution for B_{anc} is always a real probability distribution if the
 370 number of specimens is greater than one. We use a uniform prior between 0 and 250 μT
 371 for $P(B_{anc})$ as intensity values can never be negative and in databases such as the MagIC
 372 database (Tauxe et al., 2016) or the PINT database of (Biggin, 2010) rarely (if ever) ex-
 373 ceed 250 μT . For $P(\sigma_{site})$ we use a normal distribution with zero mean and standard
 374 deviation of 5 μT , truncated to always be positive.

375 Figure 5b shows our median estimates for B_m and \vec{k}_m after applying the linear restric-
 376 tion. Here, there is a tradeoff between fitting the Arai plot data with the circle, and
 377 fitting the linear trend at a site level. The effect of the linear fitting is apparent when
 378 compared to estimating \vec{k}_m and B_m for each specimen in isolation, which is shown in
 379 Figure 5a. With the linear restriction, the \vec{k} and B_m of specimens are “pulled” closer
 380 to a linear trend by modifying the Arai plot fits; specimens with more uncertain \vec{k}_m are
 381 more strongly affected (e.g., specimen labeled e) and f) in Figure 5a and b). The spec-
 382 imens with highly linear Arai plots (for which we have small uncertainty in \vec{k}_m), the cir-
 383 cle fits (see g and h) are mostly unchanged. Despite this modification of the circle fits
 384 to the Arai plots by the linear model, the circle fits to those specimens do not look un-
 385 reasonable.

386 2.3 Metrics of success

387 In order to ‘ground-truth’ the method, we rely on a compilation of paleointensity
 388 data updated from that of Paterson et al. (2014) and Tauxe et al. (2016). This compi-
 389 lation has data from 30 sites for which B_{anc} is well constrained (hence we use B_{exp}), ei-
 390 ther through the IGRF, or because the specimens were given TRMs in a known lab field
 391 before the Thellier experiment. A list of sites used here is given in Table 1. Instead of
 392 choosing a range of temperatures for each site, we simply use every temperature on the
 393 Arai plot for all specimens.

394 Because we have to estimate multiple parameters for each specimen, our method
 395 involves a high dimensional optimization problem. Therefore, we generate the estimates
 396 for B_{anc} for a given site using a Markov chain Monte Carlo (MCMC) method which ap-
 397 proximates the posterior distribution by generating pseudosamples from it (see Appendix 6.2
 398 for details). MCMC techniques are frequently used to solve high dimensional problems
 399 of this kind.

400 For each site, we quantify the effectiveness of the BiCEP method using several met-
 401 rics, f_{prob} , Δ_{median} (see Figure 6 for graphical representation), \bar{f}_{prob} , and n_{acc} :

- 402 1. f_{prob} : We report the median value of our posterior distribution and the 2.5th and
 403 97.5th percentile of the Monte Carlo sample (95% credible interval) as error bars.
 404 To quantify the effectiveness of our method, we look at the proportion of the pos-
 405 terior distribution that lies within 3 μT of the expected value of B (B_{exp}) and call
 406 this proportion f_{prob} .
- 407 2. \bar{f}_{prob} : the mean value of f_{prob} over all sites included in the study. A value of 1 is
 408 the best possible value and means all our results are accurate and precise to bet-
 409 ter than 3 μT .
- 410 3. Δ_{median} : the difference (in μT) between the median value of the MCMC sample
 411 (see Section 6.2 for explanation) and B_{exp} . The median value of Δ_{median} is $\tilde{\Delta}_{median}$.
 412 Values of $\tilde{\Delta}_{median}$ close to zero are best.
- 413 4. n_{acc} : the number of sites for which B_{exp} lies within our 95% credible interval. A
 414 related parameter, f_{acc} is the fraction of results that are accurate (n_{acc}/M), where

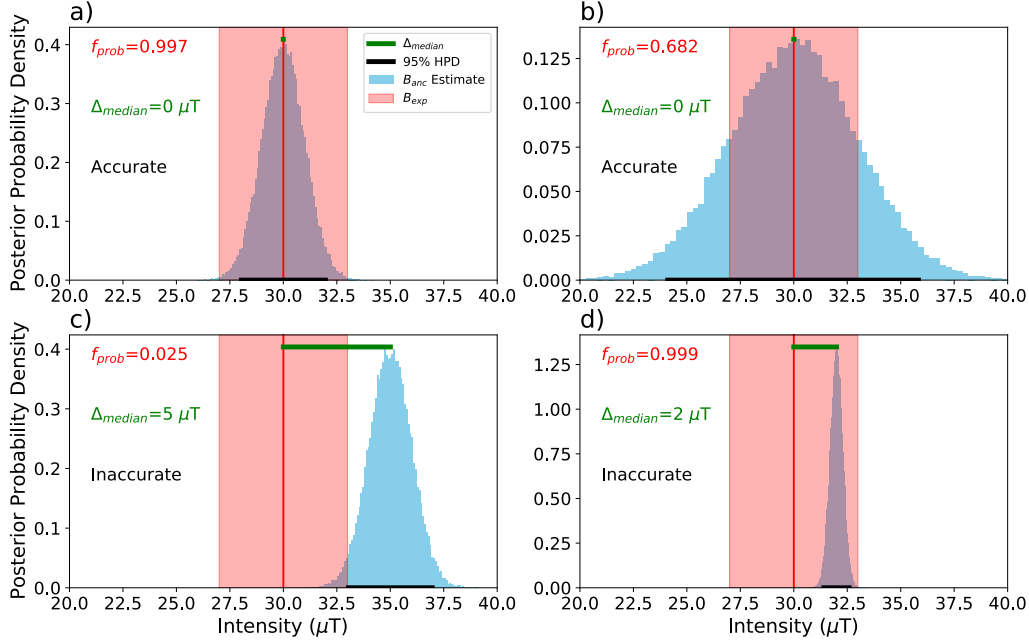


Figure 6. Examples of accuracy and precision metrics used in this study with simulated Gaussian distributions of B_{anc} for illustration. a) An accurate and precise estimate, b) An accurate but imprecise estimate, c) An inaccurate and imprecise estimate. d) A slightly inaccurate and highly precise estimate. Accuracy check used for n_{acc} checks whether the black line intersects the expected value (B_{exp}). f_{prob} is the area of the blue histogram that lies within the red shaded area. Δ_{median} is the length of the green line.

415 M is the number at the site level. We expect this number to be 0.95 in ideal cir-
 416 cumstances.

417 We use these metrics to compare the BiCEP results to those obtained by two different
 418 sets of selection criteria: CCRIT (Cromwell et al., 2015) and Paterson’s modified PICRIT03
 419 criteria (Paterson et al., 2014) (here called PICRITMOD) without the curvature param-
 420 eter \vec{k} . Most sets of commonly used selection criteria rely on an assumption of a Gaus-
 421 sian probability distribution for the site level estimate B_{anc} , which allows us to calcu-
 422 late these same metrics. For this analysis, we exclude sites that contain fewer than three
 423 specimens, or those for which have one or fewer specimens that meet any of the selec-
 424 tion criteria in CCRIT or PICRITMOD. We discuss the results of this comparison in Sec-
 425 tion 3.1.

426 2.4 Width of prior and order of fit

427 Here we consider several alternative contingent models in order to explore our choices
 428 for $P(\sigma_{site})$ and assumptions about the relationship of B_m and \vec{k} . In addition to using
 429 a standard deviation of $5 \mu\text{T}$ for $P(\sigma_{site})$, we use standard deviations of $10 \mu\text{T}$ and 20
 430 μT . The effect of this is hard to conceptualize, but wider priors will prioritize fitting cir-
 431 cles to the individual specimens over fitting the linear relationship between B_m and \vec{k}_m
 432 at a site level. The practical effect of this is wider posteriors for sites where the num-
 433 ber of specimens is small.

434 So far, we have assumed *a priori* that B_m is linearly dependent on \vec{k}_m . Because
 435 there is no theoretical reason why this should be the case, we test models for which the
 436 relationship between B_m and \vec{k}_m is described by a quadratic polynomial and a cubic poly-
 437 nomial. We would expect a higher order model to more closely fit the individual \vec{k}_m and
 438 B_m values, but with a loss of precision due to the more complicated model.

439 Results for our method, as well as for two sets of selection criteria, are given in Ta-
 440 ble 2. For each model, we calculate \bar{f}_{prob} , $\bar{\Delta}_{median}$ and f_{acc} for comparison. In this ta-
 441 ble, our models are named for the value of the standard deviation of $P(\sigma_{site})$ as well as
 442 the order of the fit. Our preferred model is referred to as “Linear 5 μ T”, and this is the
 443 model used in this paper where otherwise unspecified.

444 2.5 MCMC sampler diagnostics

445 MCMC samplers are only ever an approximation of the posterior distribution, and
 446 the number of Monte Carlo samples needed to make an accurate approximation is not
 447 the same for every site, or every run of the sampler. To determine whether we are ac-
 448 curately sampling the posterior distribution, we look at three diagnostics which are also
 449 described in Appendix 6.2:

- 450 1. \hat{R} : (Gelman & Rubin, 1992) quantifies convergence between chains in the MCMC
 451 method. This parameter is required to be between 1.1 and 0.9 for the sampler to
 452 converge.
- 453 2. n_{eff} : the effective MCMC sample size. We are using 30,000 Monte Carlo samples
 454 and n_{eff} should be large (> 1000) to have a good representation of our param-
 455 eters.
- 456 3. f_{div} : the proportion of divergent transitions f_{div} in the MCMC sample. This should
 457 ideally be zero, but it does not appear to cause large problems for the estimate
 458 of B_{anc} if it is non zero (see Section 6.2).

459 The diagnostics n_{eff} and \hat{R} are produced for each of our parameters (each of our
 460 B_m , \vec{k}_m , D_m and B_{anc} , σ_{site}). When reporting these values, we look at the worst value
 461 of \hat{R} (furthest from unity) and the value of n_{eff} for B_{anc} . If $\hat{R} > 1.1$, we replace the dis-
 462 tribution on B_{anc} with a uniform distribution between 0 and 250 μ T (the prior). The
 463 results of the MCMC sampler are presented in Section 3.4.

464 3 Results

465 3.1 Comparison of BiCEP to CCRIT and PICRITMOD

466 In this section, we compare the BiCEP to the CCRIT and PICRITMOD sets of
 467 selection criteria (see Section 2.3). The full set of results for all sites can be seen in Fig-
 468 ure 7, and are summarized in Table 3.

469 Figure 7 shows the 95% credible intervals for each method, normalized by the ex-
 470 pected value at the site. The median values of our results are generally similar to those
 471 found by CCRIT and PICRITMOD. Results from BiCEP were the most accurate, fol-
 472 lowed by CCRIT and PICRITMOD. BiCEP and PICRITMOD achieved similar levels
 473 of precision, with CCRIT’s results being slightly less precise. This indicates that our method
 474 achieves its goal of eliminating the bias introduced by poor quality specimens at least
 475 as well as selection criteria without having to exclude those specimens from the analy-
 476 sis based on arbitrarily chosen threshold values.

477 Sites in Figure 7 are sorted by the number of specimens used by BiCEP for the anal-
 478 ysis. Unique to our method, sites with low numbers of specimens (M) have wide cred-
 479 ible intervals and sites with high M have narrow credible intervals, so the estimate of

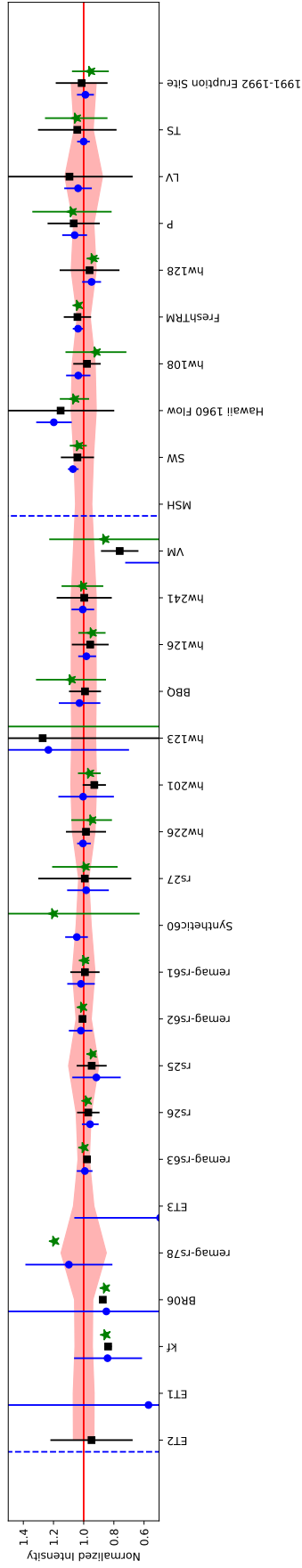


Figure 7. Paleointensity estimates for our collection of sites (Table 1) using our method (blue circles) with 95% confidence interval compared to results using CCRIT (red diamonds) and Paterson’s modified PICRITMOD (green stars). A dashed blue line indicates a site where the sampler failed with $\hat{R} > 1.1$, so the prior distribution (a uniform distribution between 0 and $250 \mu\text{T}$) was used. The results are normalized to the expected field value for each site (black line, by definition 1) and the pink shaded region represents $\pm 3 \mu\text{T}$. Sites are ordered by the number of specimens used by our method for paleointensity analysis in that site. Results are summarized in Table 3

Model Name	\bar{f}_{prob}	$\tilde{\Delta}_{median}$ (μT)	f_{acc}
Linear, 5 μT	0.67	1.5	0.80
Linear, 10 μT	0.65	1.4	0.80
Linear, 20 μT	0.65	1.5	0.80
Quadratic, 5 μT	0.60	1.6	0.75
Quadratic, 10 μT	0.59	1.7	0.80
Quadratic, 20 μT	0.59	1.6	0.80
Cubic, 5 μT	0.47	2.3	0.85
Cubic, 10 μT	0.40	3.3	0.80
Cubic 20 μT	0.40	3.9	0.90
CCRIT	0.59	1.7	0.90
PICRIT (Modified)	0.67	2.1	0.80

Table 2. Results comparing the models used in this study to results using CCRIT (Cromwell et al., 2015) and PICRITMOD (Paterson et al., 2014). See details in text and Figure 6 for explanations of the different parameters presented here. Results are sorted by the number of specimens in the site used to make the estimate using our method.

480 B_{anc} becomes more precise as more specimens are measured. This is because calculating
 481 the credible interval for a B_{anc} is more similar to calculating the standard error of
 482 the mean than the site level standard deviation, which is done for CCRIT and PICRIT-
 483 MOD.

484 The increasing precision on B_{anc} leads to some sites with high M having estimates
 485 of B_{anc} which are seemingly too precise. These estimates are still generally only a few
 486 μT away from the expected value, however, and we discuss potential reasons for this in
 487 Section 4.3.

488 Our increased level of accuracy and precision relative to CCRIT is demonstrated
 489 in our metrics (Table 2). We see that BiCEP has a higher \bar{f}_{prob} (0.67 vs 0.59) and $\tilde{\Delta}_{median}$
 490 (about 1.7 μT vs 1.5 μT), although a difference of 0.2 μT is not particularly significant.
 491 The sites which are overly precise are reflected in BiCEP’s lower f_{acc} (0.80 vs 0.90). PI-
 492 CRITMOD achieved a similar \bar{f}_{prob} to our method (also 0.67). This is probably because
 493 it is a looser set of criteria, which means there are more interpretations to pick from to
 494 optimize the standard deviation.

495 3.2 Width of the prior

496 To investigate the role of the prior distribution ($P(\sigma_{site})$), we apply the BiCEP method
 497 on the data compilation using a variety of values for its standard deviation (see Table 2).
 498 The main effect of varying σ_{site} is that for smaller values, the estimates of B_m and \vec{k}_m
 499 for specimens are “pulled” closer to the line being fitted at a site level (see Figure 5a,b).
 500 For our estimate of B_{anc} , this means that sites with fewer specimens will be more pre-
 501 cise, as it is unlikely that specimen B_m will deviate strongly from the mean. For sites
 502 with many specimens, there is little effect as σ_{site} is well constrained by the data.

503 From Table 2, we see that changes to $P(\sigma_{site})$ seem to have little influence on the
 504 effectiveness of the model, as all our f_{acc} values are the same for our linear model regard-
 505 less of the prior distribution used. We can also see graphically in Figure 7 that our pre-
 506 cision is low for these sites. Because of this, we favor the version of the model with a 5
 507 μT standard deviation on $P(\sigma_{site})$, as models with higher standard deviations reduce
 508 precision without capturing any more sites within their 95% credible intervals.

Table 3. Results for each site, including the value of f_{prob} using our method (BiCEP, superscript ‘B’) and two different sets of selection criteria, (CCRIT, superscript ‘C’) and PICRITMOD, superscript ‘P’).

Site Name	B_{exp}	M^B	B_{min}^B	B_{med}^B	B_{max}^B	f_{prob}^B	B_{med}^C	B_{min}^C	B_{max}^C	f_{prob}^C	B_{med}^P	B_{min}^P	B_{max}^P	f_{prob}^P
1991-1992 Eruption Site	36.2	53	33.9	35.8	37.6	1.00	36.7	30.7	42.7	0.67	34.6	30.4	38.8	0.73
hw108	39.3	23	37.8	40.7	43.7	0.86	38.4	35.1	41.8	0.89	36.1	28.4	43.8	0.43
hw123	37.7	12	26.6	46.5	62.9	0.15	48.0	-10.7	106.6	0.08	63.4	9.56	117.3	0.06
hw126	36.4	13	33.6	35.8	37.5	0.98	34.8	30.6	39.1	0.73	34.4	31.3	37.5	0.74
hw128	36.2	26	32.2	34.3	36.4	0.86	34.8	27.8	41.8	0.57	34.0	32.7	35.3	0.89
hw201	35.2	12	28.3	35.3	40.9	0.68	32.7	30.2	35.2	0.66	33.9	31.4	36.3	0.91
hw226	39.9	11	38.2	40.1	41.4	1.00	39.3	34.2	44.4	0.75	37.8	32.6	43.0	0.61
hw241	36.0	18	33.7	36.2	38.7	0.98	35.9	29.5	42.3	0.65	36.3	31.5	41.1	0.79
BR06	49.7	3	16.5	42.2	85.6	0.11	43.4	43.4	43.4	0.00	42.6	42.6	42.6	0.00
P	44.6	36	43.9	47.3	50.7	0.58	47.5	40.1	55.0	0.45	48.1	36.6	59.5	0.34
VM	43.8	18	4.0	18.7	31.5	0.00	33.3	28.1	38.5	0.00	37.7	21.9	53.6	0.22
BBQ	36.2	12	32.4	37.2	42.0	0.76	35.9	32.2	39.5	0.90	39.2	31.0	47.4	0.43
rs25	30.0	5	22.8	27.5	32.1	0.60	28.4	25.6	31.2	0.84	28.3	27.7	29.0	1.00
rs26	60.0	5	54.4	57.5	60.4	0.66	58.2	54.0	62.3	0.70	58.6	58.6	58.7	1.00
rs27	90.0	10	75.7	88.5	99.4	0.43	89.3	62.1	116.6	0.17	89.3	70.2	108.3	0.25
remag-rs61	40.0	6	37.3	40.7	44.1	0.91	39.7	36.0	43.3	0.89	39.8	38.7	40.9	1.00
remag-rs62	60.0	6	56.9	61.1	65.6	0.82	60.5	60.5	60.5	N/A	60.5	60.4	60.7	1.00
remag-rs63	80.0	5	75.8	79.4	83.2	0.90	78.2	78.0	78.5	1.0	79.9	79.5	80.1	1.00
remag-rs78	20.0	4	16.3	22.0	27.6	0.66	N/A	N/A	N/A	N/A	23.9	23.9	23.9	0.00
kf	52.0	3	32.2	43.8	55.0	0.05	43.6	42.6	44.5	0.00	44.4	44.3	44.5	0.00
Hawaii 1960 Flow	36.0	22	39.0	43.1	47.1	0.02	41.5	28.9	54.1	0.26	38.2	34.9	41.5	0.69
SW	46.4	19	48.2	49.7	51.0	0.33	48.3	43.5	53.2	0.65	48.1	45.7	50.4	0.87
TS	47.8	53	46.1	47.8	49.6	1.00	49.8	37.7	62.0	0.36	50.2	40.5	59.8	0.42
ET1	43.3	3	3.7	24.7	106.3	0.04	N/A	N/A	N/A	N/A	N/A	N/A	N/A	N/A
ET2	44.1	2	6.2	125.0	243.7	0.02	42.0	30.0	53.6	0.36	N/A	N/A	N/A	N/A
ET3	44.2	4	2.3	21.8	46.7	0.03	N/A	N/A	N/A	N/A	N/A	N/A	N/A	N/A
Synthetic60	60.0	7	58.7	62.8	67.0	0.55	N/A	N/A	N/A	N/A	72.0	38.1	106.0	0.11
LV	24.0	45	22.8	24.9	27.0	0.98	26.3	16.3	36.2	0.41	N/A	N/A	N/A	N/A
MSH	55.6	19	6.1	124.6	243.9	0.02	N/A	N/A	N/A	N/A	N/A	N/A	N/A	N/A
FreshTRM	70.0	24	70.7	72.6	74.7	0.65	72.9	66.9	78.9	0.49	72.5	72.0	73.1	0.96

509

3.3 Order of polynomial fit

510

511

512

513

514

515

The results for our test sites (Table 2) demonstrate that increasing the order of the polynomial fit significantly decreases the precision of the estimate as demonstrated by reduced values of \hat{f}_{prob} . This is expected as there are more parameters to be estimated with the same number of data. The level of accuracy is also reduced, with $\hat{\Delta}_{median}$ increasing as the order of the fit increases. For this reason, we assume a linear relationship between B_m and \vec{k}_m .

516

3.4 Sampler Diagnostics

Site Name	Worst \hat{R}	n_{eff}	f_{div}
1991-1992 Eruption Site	1.00	59741	0.00
hw108	1.00	77959	0.00
hw123	1.01	11687	0.00
hw126	1.00	36130	0.01
hw128	1.00	78978	0.00
hw201	1.00	10641	0.01
hw226	1.00	7139	0.05
hw241	1.00	66565	0.00
BR06	1.01	451	0.00
P	1.00	62252	0.00
VM	1.05	1447	0.00
BBQ	1.00	63082	0.00
rs25	1.00	5614	0.00
rs26	1.00	11866	0.00
rs27	1.00	22211	0.00
remag-rs61	1.00	26746	0.00
remag-rs62	1.00	16916	0.00
remag-rs63	1.00	3788	0.00
remag-rs78	1.00	12388	0.00
kf	1.02	2712	0.00
Hawaii 1960 Flow	1.00	60184	0.00
SW	1.00	36390	0.00
TS	1.00	56518	0.00
ET1	1.01	995	0.00
ET2	6.93	6	0.03
ET3	1.01	424	0.00
Synthetic60	1.00	36572	0.01
LV	1.02	5931	0.08
MSH	2.78	24	0.45
FreshTRM	1.00	81007	0.00

Table 4. Sampler diagnostics (see Section 2.5 for an explanation of each diagnostic) for each site using the BiCEP method.

517

518

519

520

521

522

The sampler diagnostics for each site are given in Table 4. Indicators of poor MCMC sampler performance (worst $\hat{R} > 1.1$, low n_{eff} , high f_{div}) tend to occur at sites with four or fewer specimens, or sites where the Arai plots are extremely scattered and the sampler struggles to fit them. This indicates that to get a strongly reproducible answer from this method, paleomagnetists ought to measure five or more specimens per site. In practice, most studies already do this in order to have enough specimens that pass the cho-

523 sen selection criteria, yet many specimens may be excluded from analysis. Here, we can
 524 use all of the specimens measured so there may be no additional burden.

525 3.5 Summary of Results

526 After testing all of our contingent models, we prefer the model which assumes the
 527 relationship between B_m and \vec{k}_m is linear, and which uses a $5 \mu\text{T}$ standard deviation on
 528 $P(\sigma_{site})$. This model has a higher level of accuracy than the PICRIT and CCRIT sets
 529 of selection criteria and higher precision than CCRIT. Our precision increases for sites
 530 for which the number of specimens is large, similarly to calculating the standard error
 531 of the mean when using selection criteria. Unlike selection criteria, the BiCEP method
 532 does not require exclusion of large numbers of specimens to obtain an accurate result,
 533 which leads us to prefer it over those methods.

534 4 Discussion

535 4.1 Advantages of BiCEP compared to selection criteria

536 BiCEP has significant advantages over classical selection criteria. Firstly, we ob-
 537 tain estimates for all sites with at least three specimens, including some which do not
 538 contain any specimens that pass classical selection criteria, see Figure 7. In most cases,
 539 our estimates have give similar or higher accuracy than the selection criteria (evidenced
 540 by $\hat{\Delta}_{median}$ and Figure 7), and this is accomplished while only excluding specimens from
 541 the analysis which were not fully demagnetized.

542 Secondly, the increasing precision of our paleointensity estimate as the number of
 543 specimens increases allows for an improved workflow when compared to classical paleo-
 544 ointensity criteria. Instead of needing a minimum number of specimens to pass our se-
 545 lection criteria, we can keep measuring specimens until we reach a desired level of pre-
 546 cision. We discuss this workflow in more detail in Section 4.2. The property of increas-
 547 ing precision with number of specimens is inherent to Bayesian models and can also be
 548 found in the method of Kosareva et al. (2020), although this method does not include
 549 the bias correction found in our method.

550 Thirdly, our method propagates the uncertainties from a specimen to the site level.
 551 Specimens with more scattered (or non linear, or non circular) Arai plots will have less
 552 influence over the specimen mean than those with highly linear Arai plots. In addition
 553 to this, the BiCEP method foregoes the need for criteria which are concerned with the
 554 length of the line on the Arai plot used to make an interpretation, like the NRM Frac-
 555 tion (e.g., FRAC of Shaar & Tauxe, 2013). Using a set of temperatures with small FRAC
 556 will cause an increase in the uncertainty in \vec{k} (see Figure 4e, f), which will cause this spec-
 557 imen to have less effect on the estimate of B_{anc} , without excluding it from the analy-
 558 sis entirely. We discuss this further in Section 4.4.

559 4.2 Workflow with BiCEP

560 Figure 8 plots precision (here expressed as the full width of the 95% credible
 561 interval as a percentage of the median) against the number of specimens per site (M).
 562 The use of the 95% credible interval in BiCEP differs from the use of the standard er-
 563 ror of the mean with selection criteria in that relying on the standard error generally leads
 564 to overly precise measurements in the frequent case of low numbers of specimens ($M <$
 565 5).

566 We have divided Figure 8a and b into four regions (A-D). Region A has high pre-
 567 cision with many specimens. Region B has high precision (better than 40%, which for
 568 a Gaussian distribution would be equivalent to a standard deviation of $\pm 10\%$) with few

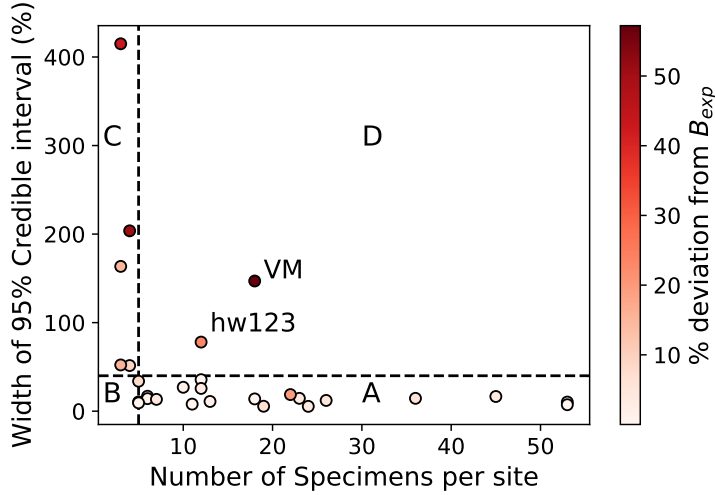


Figure 8. Plot of precision of estimates using the Linear, BiCEP against the number of specimens per site for all sites where $\hat{R} < 1.1$. Colors indicate the deviation of the median value of the estimate from the expected site value (B_{exp}) as a percentage. The horizontal dashed line indicates a value of 40% for the full width of the 95% credible interval, which for a Gaussian distribution would correspond to a standard deviation of $\pm 10\%$. Suggested workflow for sites in regions: A) Accept the site. B) Continue measuring if better precision is desired, if not, accept the site as is. C) Continue measuring specimens, as improved precision is likely. D) Stop measuring the site as further effort is likely to be futile.

specimens ($M < 5$). Region C has low precision but a low number of specimens ($M < 5$) and Region D has similarly poor precision but a large number of specimens ($M > 5$). With few exceptions (VM, hw123), the BiCEP method allows for increasing precision in the estimate of B_{anc} as the number of specimens increases. For sites where the median value for the intensity is low, it may be more appropriate to define these regions using an absolute width for the intensity bound rather than a percentage.

Because all of the sites considered here have known values for the site intensity, we can also consider accuracy. From Figure 8, we see that almost all sites with an estimated precision better than 40% have median values within 20% of B_{exp} , as might be expected. (color of dots reflect the deviation from B_{exp}). Considering the region in which a particular site plots leads to a workflow based on the likelihood of success. For sites in Region C, obtaining more specimens is likely to result in improved precision and accuracy. If after measuring more specimens, a site may move from region C into region D (e.g., sites hw123 and VM) and further effort is likely to be futile. If a site moves from region C into regions A or B, the site may be acceptable, depending on the desired precision. If a higher level of precision is desired (better than 40%), increasing M is likely to be successful.

4.3 Overly precise estimates of B_{anc}

The BiCEP method has a lower f_{acc} than CCRIT, despite having a similar degree of accuracy when using a metric like Δ_{median} . The reason for this is that the increasing precision on the BiCEP estimate leads to estimates which are highly precise when M is large. This is the case shown in Figure 6d.

591 Labeling sites with extremely high precision in the estimate may be misleading, as
 592 we have not taken into account uncertainties in the value of the expected fields at the
 593 sites in this study. For example, using differences between the observed directions and
 594 the IGRF, Yamamoto and Hoshi (2008) quoted the expected value at the site “SW” as
 595 $46.0 \pm 2.6 \mu\text{T}$, which is just consistent with the 95% credible interval for our specimen
 596 ($48.2\text{--}49.7 \mu\text{T}$). Because of this, we prefer to use \bar{f}_{prob} as a metric of how well a model
 597 performs as it allows for a few μT of uncertainty in the expected field value. Addition-
 598 ally, Yamamoto and Yamaoka (2018) suggested that the IZZI-Thellier results for sites
 599 SW and TS may be biased slightly high due to acquisition of a thermo-chemical reman-
 600 ent magnetization (TCRM), which is not detectable by our method. Yamamoto et al.
 601 (2003) also invoke a TCRM mechanism to explain the paleointensity overestimate for
 602 the Hawaii 1960 Flow, which is another of their sites for which we overestimate the ex-
 603 pected intensity (see Table 3). We note that Cromwell et al. (2015) also sampled the 1960
 604 flow (hw241 which targeted the fine grained flow top) and all selection criteria resulted
 605 in accurate results, with BiCEP producing the tightest confidence interval.

606 4.4 Exclusion of measurement level data

607 It is frequently possible to improve the accuracy and precision of results by find-
 608 ing the ‘best’ set of temperature steps to use in the intensity interpretation. Two situ-
 609 ations frequently occur for which this might be justified. The first is the case in which
 610 thermochemical alteration occurs at high temperature (e.g., Figure 4e). For such spec-
 611 imens, the low temperature measurements can be used to make a paleointensity estimate
 612 (colored dots in the figure). Figures 4e and f show how our method can be used on a re-
 613 duced range of temperature steps on the Arai plot at the cost of precision. The plot of
 614 circle fits (green lines in Figure 4e) demonstrates that the Arai plot interpretations are
 615 poorly constrained and can continue in any direction after the last temperature step cho-
 616 sen. This results in a higher uncertainty in the curvature associated with this (Figure 4f).
 617 The second case in which a portion of the data could be excluded from the calculation,
 618 would be when the magnetization has multiple components (Figure 9a). In such a case,
 619 a paleointensity estimate can only be made using the small range of temperature steps
 620 that correspond to the characteristic component. We currently do not have an objec-
 621 tive method to choose which set of temperature steps on the Arai plot to use. We sug-
 622 gest that decisions about which data points to include should not be made based on the
 623 original in-field or zero field Arai plot measurements (dots in the Arai plots), but rather
 624 exclusively on deviating pTRM checks (triangles in, e.g., Figure 4e) or other indicators
 625 of alteration for the first case and on the directions of the magnetization vector (it must
 626 trend to the origin and be well defined) in the second case, e.g., Figure 9a.

627 4.5 Application to multi-component magnetizations

628 We test an application of the BiCEP method on data with multi-component di-
 629 rections as shown in Figure 9a using the data of Lisé-Pronovost et al. (2020). The data
 630 are from Scottish firebricks which were used in a foundry in Australia. The date and lo-
 631 cation of firing are both well constrained, hence we have a reasonably well constrained
 632 value for B_{exp} . The bricks all contained a low temperature component associated with
 633 the Australian field. Some also displayed a high temperature component associated with
 634 the original firing in Scotland as shown in Figure 9a. Lisé-Pronovost et al. (2020) already
 635 have interpretations which separate these components in the original study. To account
 636 for the change in direction of the NRM, we subtract the high temperature component
 637 from the low temperature component, and then add the magnitude of these values to
 638 the magnitude of the low temperature component (see Figure 9 for a graphical expla-
 639 nation). The vector subtraction is necessary for the low-temperature component as we
 640 need a total TRM ($p\text{TRM}_{max}$) to scale by in order to penalize the result for shorter com-
 641 ponents. We then proceed to use the BiCEP method as previously described, using the

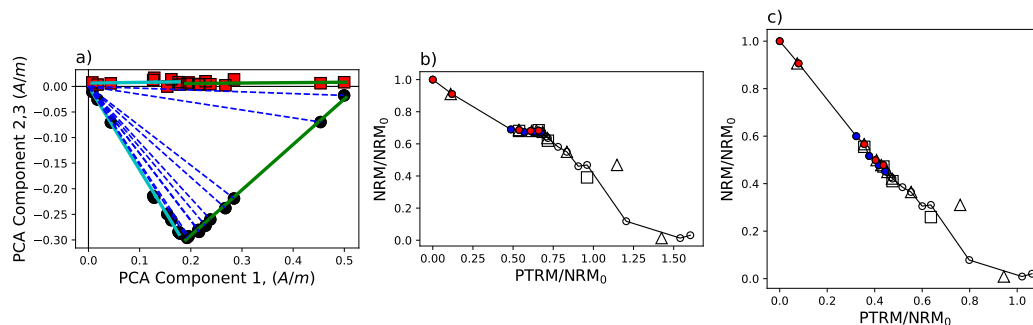


Figure 9. a) Example of vector endpoint diagram for specimen FB2-B1 from Lisé-Pronovost et al. (2020). The magnetization is rotated so that the principal component of the TRM direction for all steps lies along the x axis. Green line fit to the low temperature component and cyan line fit to the high temperature component. b) Arai plot and c) “corrected” Arai plot for a specimen from the data shown in b). NRM values for the low temperature component (filled circles) are calculated by taking the magnitude of the vector endpoint (blue dashed lines in the vector endpoint diagram in a). In b), these NRM values are calculated by vector subtracting the high temperature component (cyan line), taking the magnitude of our new NRM vectors (distance along green line), and adding the magnitude of the low temperature component (length of cyan line).

642 original interpretations for the different components. For the sake of simplicity, we do
 643 not perform the magnetomineralogical change (MMC) correction (Valet et al., 1996). We
 644 also do not apply the corrections for anisotropy of TRM or cooling rate with these data,
 645 as they appeared to be negligible. Of course these could be applied in the usual fash-
 646 ion if necessary.

647 We display the results from multi-component remanences in Figure 10. We find that
 648 for the low temperature, Australian field, component (Figure 10a), our estimates for all
 649 firebricks contain the expected answer ($61.17 \mu\text{T}$) within the 95% credible interval. Our
 650 interpretation for site FBG is slightly less accurate than the original analysis but with
 651 much higher precision. This difference is likely caused by not applying the MMC cor-
 652 rection, as the specimens at this site were mostly of good quality, with none being ex-
 653 cluded from the original analysis. (Figure 10b) behaves differently.

654 The sampler does not converge for site FB1, indicating too few specimens in the
 655 analysis. For site FB2, we have a result that is less accurate, but more precise than in
 656 the original study. The lack of MMC correction may contribute to the decreased accu-
 657 racy in this example, whereas the reduced precision is likely caused by the smaller length
 658 of the interpretation on the Arai plot, leading to a higher uncertainty in the curvature
 659 for that specimen. Our results for this study demonstrate that BiCEP will be effective
 660 for obtaining precise estimates for components which represent most of the magnetiza-
 661 tion, and ineffective for components which have small NRM fraction.

662 4.6 Implications for bias in curved Arai plots

663 The success of our method demonstrates that Arai plot “curvature” or sagging does
 664 lead to a progressive bias in paleointensity estimation which increases as the amount of
 665 curvature increases as described by Tauxe et al. (2021) and strongly suggested by the
 666 data of Krása et al. (2003) (see Figure 1). Our estimates are made by using the tangent
 667 to a circle fit rather than fitting a line to part of the data, so one might expect them to

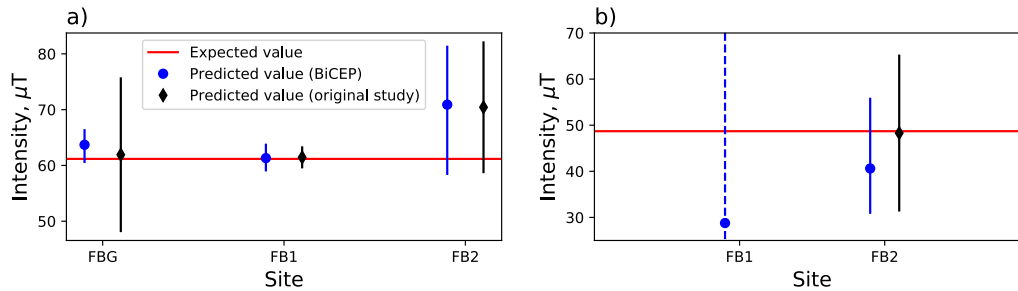


Figure 10. Expected and predicted intensities on the data of Lisé-Pronovost et al. (2020) using BiCEP (blue circles) and the method used in the original study (black diamonds). a) Results for the low temperature component (Australia, expected field value $61.17 \mu\text{T}$) for each firebrick. b) Results for the high temperature component (Scotland, expected field value $48.3 \mu\text{T}$), where this component was present. The dashed blue line indicates that the MCMC sampler failed to converge for site FB1.

668 be biased. However, it has been demonstrated by e.g. the data of (Krása et al., 2003)
 669 that fitting lines to the high temperature or low temperature slope of Arai plots yields
 670 even more biased results. Fitting a tangent gives a result more similar to the best fit-
 671 ting line to all data, or the total TRM, both of which exhibit a similar progressive bias
 672 for curved Arai plots. The bias seen generally underestimates paleointensity with higher
 673 (positive) curvature, but this is not the case for all sites, some of which exhibit the op-
 674 posite trend.

675 The assumption of a quasi-linear dependence between the specimen level paleoin-
 676 tensities and the curvature of the Arai plot does not have any theoretical basis. We stress
 677 that this relationship only needs to be loosely followed for our method to work. In cases
 678 where there does not appear to be a strong linear relationship between B_m and \vec{k}_m (e.g.
 679 in Figure 2c), an accurate paleointensity estimate is still possible if there are enough spec-
 680 imens with low $|\vec{k}|$, as the intercept of the linear fit is still well constrained even if the
 681 slope is not. Conversely, if there are few specimens with high $|\vec{k}|$ and there is a poor lin-
 682 ear relationship, then both the slope and intercept are poorly constrained, resulting in
 683 a huge uncertainty in B_{anc} .

684 5 Conclusions

- 685 • We present a new Bayesian method (BiCEP) which accounts for bias in paleoin-
 686 tensity estimates in specimens.
- 687 • Instead of excluding specimens from the paleointensity analysis in the traditional
 688 (binary) selection criteria based approach, our method predicts an amount of bias
 689 for each specimen, using the curvature of the Arai plot as a metric of non-linearity
 690 and a predictor of bias. In this way, the BiCEP method is quite different from the
 691 recently published Bayesian approach of Kosareva et al. (2020).
- 692 • When tested on a compilation of sites for which an approximate paleointensity is
 693 known *a priori*, our method is more accurate than two commonly used sets of se-
 694 lection criteria, and has a similar level of accuracy to the modified PICRIT cri-
 695 teria of Paterson et al. (2014).
- 696 • Our method generates some slightly inaccurate paleointensity estimates with high
 697 levels of precision, but these can generally be explained with inaccuracies in the
 698 expected field (see Section 4.3).

- 699 • The BiCEP method handles uncertainties in a different way than using classical
700 selection criteria, as the uncertainty in site level estimates decreases as the num-
701 ber of specimens increases, but this uncertainty remains high when the number
702 of specimens is low due to inclusion of prior information. The Bayesian uncertain-
703 ties are in this way more similar to the ‘extended error bars’ in the Thellier_GUI
704 auto-interpreter of Shaar and Tauxe (2013).
- 705 • We propose a workflow in which sites are accepted and measurement of specimens
706 can cease once a desired level of confidence in the site level estimate has been reached.
707 Sites which do not reach this level of confidence after measuring several (> 5) spec-
708 imens likely do not contain useful information and can be discarded.

709 Data Availability Statement

710 Data used in this paper may be found in the MagIC database at: [https://earthref](https://earthref.org/MagIC/17104/0326fdaa-4bcf-44f3-989d-0116b9a2fb75)
711 [.org/MagIC/17104/0326fdaa-4bcf-44f3-989d-0116b9a2fb75](https://earthref.org/MagIC/17104/0326fdaa-4bcf-44f3-989d-0116b9a2fb75) for review and will be
712 available to the public at <https://earthref.org/MagIC/17104> on publication.

713 6 Appendix

714 6.1 Change of variables

715 In Section 2.2.1 we mention that we need to use a change of variables to get from
716 our original circle fitting parameters R, x_c, y_c to our new set of parameters \vec{k}, D, ϕ . We
717 can use the Jacobian of the parameter change to get the new formula for the posterior
718 probability under our new parameters:

$$P(D, \phi, \vec{k}|x, y) = P(x_c, y_c, R|x, y) \left| \frac{\partial(x_c, y_c, R)}{\partial(D, \phi, \vec{k})} \right|. \quad (20)$$

719 We can evaluate this Jacobian as:

$$\left| \frac{\partial(x_c, y_c, R)}{\partial(D, \phi, \vec{k})} \right| = \left| \frac{\vec{k}}{|\vec{k}^3|} \left(D + \frac{1}{\vec{k}} \right) (\cos \phi + \sin \phi) \right|. \quad (21)$$

720 So our posterior looks like:

$$P(D, \phi, \vec{k}|x, y) \propto \left(\sum_{n=1}^N \sqrt{\left(\left(D + \frac{1}{\vec{k}} \cos \theta \right) - x_n \right)^2 + \left(\left(D + \frac{1}{\vec{k}} \sin \theta \right) - y_n \right)^2 - \frac{1}{|\vec{k}|}} \right)^{-N/2}$$

$$\left| \frac{\vec{k}}{|\vec{k}^3|} \left(D + \frac{1}{\vec{k}} \right) (\cos \phi + \sin \phi) \right| P(\vec{k}, \phi, D). \quad (22)$$

722 6.2 Markov chain Monte Carlo sampling

723 The Markov chain Monte Carlo (MCMC) sampling method generates a set of sam-
724 ples from the posterior probability distribution of B_{anc} which allows us to approximate
725 it. We use the python bindings for the Stan software package (<http://mc-stan.org>) to
726 generate these samples which provides diagnostic information and runs relatively quickly.
727 For each site we run four Markov chains and generate 30,000 samples of B_{anc} in each
728 chain. We discard the first half of the chain as ‘burn in’ for a total of 60,000 samples.

729 Stan provides several diagnostics that tell us whether we have successfully sampled
730 the posterior distribution. These include the \hat{R} score (Gelman & Rubin, 1992) which tells

731 us about the convergence between chains, and is required to be between 1.1 and 0.9 which
 732 is necessary for convergence, the effective sample size, n_{eff} which should be large (> 1000)
 733 for a good sample and the number of divergent transitions (f_{div}) which should be zero
 734 in ideal cases. In most cases our results display high degrees of convergence with \hat{R} close
 735 to 1 and high effective sample sizes. Some sites included divergent transitions in small
 736 numbers. These seem to occur at a specimen level for specimens where the posterior dis-
 737 tribution of one of the circle parameters is long-tailed. In theory this can mean the pos-
 738 terior was inefficiently sampled, but because these specimens generally have large un-
 739 certainties on their k parameter, the final results do not change, even under a change of
 740 parameters. The sampler struggled to converge, with $\hat{R} > 1.1$ for several sites with very
 741 few specimens, where once again the distributions are extremely long tailed. The sam-
 742 pler also did not converge for site MSH, where the Arai plots were so non linear, with
 743 few points, that BiCEP struggled to fit circles to them. We consider these sites to have
 744 “failed” using our method (grade of ‘D’ in Figure 8) and use the prior distribution on
 745 B_{anc} (uniform between 0 and 250 μT) as an estimate of their intensity. We calculate the
 746 \hat{R} furthest from unity, the n_{eff} for B_{anc} and the proportion of divergent samples f_{div}
 747 for our model.

748 6.3 Code and GUI

749 We present a simple GUI that can perform the BiCEP method on data in the MagIC
 750 format. The code uses Jupyter notebooks and can be found at ([http://github.com/
 751 bcych/BiCEP_GUI](http://github.com/bcych/BiCEP_GUI)) and contains a readme file detailing how to use the notebook. The
 752 GUI can also be accessed at the Earthref JupyterHub site ([http://jupyterhub.earthref
 753 .org](http://jupyterhub.earthref.org)). To access the GUI this way:

- 754 • Sign up to Earthref at (<http://earthref.org>)
- 755 • Navigate to the Earthref JupyterHub site at (<http://jupyterhub.earthref.org>)
- 756 • Open and run all the cells in the “BiCEP GUI - Setup.ipynb” notebook.
- 757 • Upload MagIC formatted “sites”, “samples”, “specimens” and “measurements”
 758 files to the BiCEP_GUI directory in JupyterHub. These can be formatted using
 759 pmag_gui. (Tauxe et al., 2016).
- 760 • Open the BiCEP GUI notebook and press the “App Mode” button.

761 For more detailed instructions, read the included readme file at the github site.

762 Acknowledgments

763 We are deeply grateful for the advice given by Andrew Roberts, David Heslop and Joseph
 764 Wilson. This research was supported in part by NSF Grants EAR1547263 and EAR1827263
 765 to LT. We are also grateful to Agnes Lisé-Pronovost for sharing her measurement level
 766 data.

767 References

- 768 Biggin, A. (2010). Paleointensity database updated and upgraded. *EOS*, *91*, 15.
- 769 Chernov, N., & Lesort, C. (2005). Least squares fitting of circles. *Journal of Mathe-*
 770 *matical Imaging and Vision*, *23*(3), 239–252. doi: 10.1007/s10851-005-0482-8
- 771 Cromwell, G., Tauxe, L., Staudigel, H., & Ron, H. (2015). Paleointensity es-
 772 timates from historic and modern hawaiian lava flows using glassy basalt
 773 as a primary source material. *Phys. Earth Planet. Int.*, *241*, 44–56. doi:
 774 10.1016/j.pepi.2014.12.007
- 775 Dunlop, D., & Özdemir, O. (2001). Beyond Néel’s theories: thermal demagnetization
 776 of narrow-band partial thermoremanent magnetization. *Phys. Earth Planet.*
 777 *Int.*, *126*, 43–57.

- 778 Gelman, A., Carlin, J. B., Stern, H. S., & Rubin, D. B. (2004). *Bayesian data analysis*
779 *(Second ed.)*. Chapman & Hall/CRC, Boca Raton, FL.
- 780 Gelman, A., & Rubin, D. B. (1992, 11). Inference from iterative simulation using
781 multiple sequences. *Statist. Sci.*, 7(4), 457–472. Retrieved from [https://doi](https://doi.org/10.1214/ss/1177011136)
782 [.org/10.1214/ss/1177011136](https://doi.org/10.1214/ss/1177011136) doi: 10.1214/ss/1177011136
- 783 Hoffman, K. A., Constantine, V. L., & Morse, D. L. (1989). Determination of absolute
784 palaeointensity using a multi-specimen procedure. *Nature*, 339, 295–297.
- 785 Königsberger, J. G. (1938). Natural residual magnetism of eruptive rocks. *Ter-*
786 *restrial Magnetism and Atmospheric Electricity*, 43(3), 299–320. doi: 10.1029/
787 TE043i003p00299
- 788 Kosareva, L. R., Kuzina, D. M., Nurgaliev, D. K., Sitdikov, A. G., Luneva, O. V.,
789 Khasanov, D. I., ... Spassov, S. (2020). Archaeomagnetic investigations in Bolgar (Tatarstan). *Stud. Geophys. Geod.*, 64(2), 255–292. doi:
790 10.1007/s11200-019-0493-3
- 791 Krása, D., Heunemann, C., Leonhardt, R., & Petersen, N. (2003). Experimental
792 procedure to detect multidomain remanence during thellier–thellier experi-
793 ments. *Phys. Chem Earth (A/B/C)*, 28(16), 681 - 687. (Paleo, Rock and
794 Environmental Magnetism 2002) doi: 10.1016/S1474-7065(03)00122-0
- 795 Lisé-Pronovost, A., Mallett, T., & Herries, A. I. R. (2020). Archaeointen-
796 sity of nineteenth-century scottish firebricks from a foundry in melbourne,
797 australia: comparisons with field models and magnetic observatory data.
798 *Geological Society, London, Special Publications*, 497(1), 27–45. Re-
799 trieved from <https://sp.lyellcollection.org/content/497/1/27> doi:
800 10.1144/SP497-2019-72
- 801 Nagata, T., Arai, Y., & Momose, K. (1963). Secular variation of the geomagnetic to-
802 tal force during the last 5000 years. *J. Geophys. Res.*, 68(18), 5277–5281. doi:
803 10.1029/j.2156-2202.1963.tb00005.x
- 804 Nagy, L., Williams, W., Muxworthy, A. R., Fabian, K., Almeida, T. P., Conbhú,
805 P. Ó., & Shcherbakov, V. P. (2017). Stability of equidimensional pseudo-
806 single-domain magnetite over billion-year timescales. *Proc. Natl. Acad. Sci.*
807 *U.S.A.*, 114(39), 10356–10360. doi: 10.1073/pnas.1708344114
- 808 Néel, L. (1949). Théorie du traînage magnétique des ferromagnétiques en grains fins
809 avec applications aux terres cuites. *Ann. géophys.*, 5, 99–136.
- 810 Paterson, G. A. (2011). A simple test for the presence of multidomain be-
811 havior during paleointensity experiments. *J. Geophys. Res.*, 116. doi:
812 10.1029/2011JB008369
- 813 Paterson, G. A., Biggin, A. J., Yamamoto, Y., & Pan, Y. (2012). Towards the ro-
814 bust selection of Thellier-type paleointensity data: The influence of experimen-
815 tal noise. *Geochem. Geophys. Geosyst.*, 13(5). doi: 10.1029/2012GC004046
- 816 Paterson, G. A., Tauxe, L., Biggin, A. J., Shaar, R., & Jonestrask, L. C. (2014). On
817 improving the selection of thellier-type paleointensity data. *Geochem. Geophys.*
818 *Geosyst.*, 15(4), 1180–1192. doi: 10.1002/2013GC005135
- 819 Shaar, R., & Tauxe, L. (2013). Thellier_gui: An integrated tool for analyzing pa-
820 leointensity data from thellier-type experiments. *Geochem. Geophys. Geosys.*,
821 14, 677–692. doi: doi:10.1002/ggge.20062
- 822 Shaw, J. (1974). A new method of determining the magnitude of the paleomagnetic
823 field application to 5 historic lavas and five archeological samples. *Geophys. J.*
824 *R. astr. Soc.*, 39, 133–141.
- 825 Tauxe, L., Santos, C., Cych, B., Zhao, X., Roberts, A., Nagy, L., & Williams, W.
826 (2021). Understanding non-ideal paleointensity recording in igneous rocks:
827 Insights from aging experiments on lava samples and the causes and conse-
828 quences of 'fragile' curvature in arai plots. *Geochem. Geophys. Geosyst.*, 22,
829 e2020GC009423. doi: 10.1029/2020GC009423
- 830 Tauxe, L., Shaar, R., Jonestrask, L., Swanson-Hysell, N. L., Minnett, R., Koppers,
831 A. a. P., ... Fairchild, L. (2016). PmagPy: Software package for paleomag-

- 833 netic data analysis and a bridge to the magnetism information consortium
834 (MagIC) database. *Geochem., Geophys., Geosyst.*, 17(6), 2450–2463. doi:
835 10.1002/2016GC006307
- 836 Tauxe, L., & Yamazaki, T. (2015). Paleointensities. In M. Kono (Ed.), *Geomag-*
837 *netism* (2nd Edition ed., Vol. 5, p. 461-509). Elsevier.
- 838 Thébault, E., Finlay, C. C., Beggan, C. D., Alken, P., Aubert, J., Barrois, O., ...
839 Zvereva, T. (2015). International Geomagnetic Reference Field: the 12th
840 generation. *Earth Planets Space*, 67(1), 79. doi: 10.1186/s40623-015-0228-9
- 841 Thellier, E., & Thellier, O. (1959). Sur l'intensité du champ magnétique terrestre
842 dans le passé historique et géologique. *Ann. Geophys.*, 15, 285.
- 843 Valet, J.-P., Brassart, J., Le Meur, I., Soler, V., Quidelleur, X., Tric, E., & Gillot,
844 P.-Y. (1996). Absolute paleointensity and magnetomineralogical changes. *Jour-*
845 *nal of Geophysical Research: Solid Earth*, 101(B11), 25029-25044. Retrieved
846 from [https://agupubs.onlinelibrary.wiley.com/doi/abs/10.1029/](https://agupubs.onlinelibrary.wiley.com/doi/abs/10.1029/96JB02115)
847 [96JB02115](https://doi.org/10.1029/96JB02115) doi: <https://doi.org/10.1029/96JB02115>
- 848 Williams, W., & Dunlop, D. J. (1989). Three-dimensional micromagnetic modelling
849 of ferromagnetic domain structure. *Nature*, 337, 634–637.
- 850 Yamamoto, Y., & Hoshi, H. (2008). Paleomagnetic and rock magnetic studies of
851 the sakurajima 1914 and 1946 andesitic lavas from japan: A comparison of
852 the ltd-dht shaw and thellier paleointensity methods. *Phys. Earth and Planet.*
853 *Inter.*, 167, 118-143.
- 854 Yamamoto, Y., Tsunakawa, H., & Shibuya, H. (2003). Palaeointensity study of
855 the hawaiian 1960 lava: implications for possible causes of erroneously high
856 intensities. *Geophys J Int*, 153(1), 263-276.
- 857 Yamamoto, Y., & Yamaoka, R. (2018). Paleointensity study on the Holocene surface
858 lavas on the Island of Hawaii using the Tsunakawa-Shaw method. *Front. Earth*
859 *Sci.*, 6. doi: 10.3389/feart.2018.00048
- 860 Yu, Y., Tauxe, L., & Genevey, A. (2004). Toward an optimal geomagnetic field in-
861 tensity determination technique. *Geochem., Geophys., Geosyst.*, 5(2). doi: 10
862 .1029/2003GC000630